Self-Neutralization and Performance Characteristics of a Hypersonic Air-Breathing Plasma Thruster

IEPC-2025-119

Presented at the 39th International Electric Propulsion Conference Imperial College London • London, United Kingdom 14-19 September 2025

Anmol Taploo*, Guru Sankar Duppada, Jake Spinelli, Michael Keidar*
Micro Propulsion and Nanotechnology Laboratory, Department of Mechanical and Aerospace Engineering,
George Washington University, Washington DC 20052, USA

*Corresponding authors' emails: anmol035@gwu.edu, keidar@gwu.edu

Abstract: This paper presents a detailed assessment of the air-breathing plasma thruster with magneto-plasma-dynamic acceleration, designed for sustained operation in the upper mesospheric altitudes (65–120 km) regime. This paper also describes the mechanism of self-neutralization of positive ion charge extracted from an air-breathing plasma thruster that was studied using particle-in-cell Monte Carlo collisions simulations. To analyse plasma behaviour under different conditions, a combination of Langmuir probe, time-of-flight diagnostics, and thrust experiments was used. Experiments were performed at mass flow rates (10⁻⁷–10⁻³ kg/s) and pulse frequencies from 1–50 Hz to simulate the relevant conditions (65-120 km). Time of flight analysis confirmed high ion velocities (6-60 km/s) consistent with pulsed acceleration, while thrust and thrust-to-power ratio exceeded 1.6 N and 5 N/kW at higher flow rates, thanks to efficient inlet velocity use and reduced flow stagnation.

I. Introduction

The pursuit of efficient propulsion systems for air-breathing altitudes (<400 km) [1], [2], [3], [4], [5], [6] has intensified due to the unique advantages these altitudes offer, including improved nextgeneration Earth observation resolution (10cm resolution) [7], reduced latency for communication constellations [8], reduced radiation exposure levels (50-80% lower [9]) and natural deorbiting to mitigate space debris. However, high atmospheric drag in this regime requires continuous thrust generation for sustained orbital maintenance. Typically, thrust level (90 mN-90 N) is required to cancel drag that is (60 mN-60 N) substantial at low altitudes [10], [11], [12]. Traditional propulsion systems, reliant on onboard propellant, face limitations in lifespan, mass, and reusability. This has sparked interest in Air-Breathing Plasma Thruster (ABPT) systems, which utilize atmospheric gases as propellant, offering the potential for long-duration operation and reduced mission costs. Conventional systems, such as grid ion and Hall effect thrusters, have been widely used for higher orbits due to their high specific impulse (I_{sp}) and thrust. Grid ion thrusters use electrostatic acceleration grids to achieve an I_{SP} of 1500-4500 s. Hall thrusters rely on the $E \times B$ configuration to generate high thrust density and are compatible with small satellites. However, both thrusters depend on external cathode neutralizers and stored propellant. Additionally, the presence of grids in grid ion thrusters and magnets in Hall thrusters can lead to significant internal drag in drag-dominant upper atmospheric environments. In a high drag regime, Magnetoplasmadynamic (MPD) accelerators (thrusters) are well-suited for such environments, offering high thrust densities [13] and compatibility with reactive gases while eliminating the need for separate neutralizers [14].

Substantial experimental and modelling work has been conducted on air-breathing MPD. An air-breathing pulsed MPD-type plasma thruster (PPT) was designed by Adkins et al. [15], which achieved a thrust to power (*T/P*) of 14-16 mN/kW at 3.2hPa and 5hPa with pulse energies of 4J and 6J. Goksel and Mashek's [16], magneto-plasma compressor (MPC) achieved impulse bits of 1.2-8 mNs at discharge of 200-600V while generating high thrust densities (50-150 kN/m²). A thruster efficiency-

focused study on an air-breathing MPD thruster with existing electric propulsion systems was conducted by McKinney and Murnan [17], where models were used to estimate the thrust vs discharge current. A maximum thrust of 6.5 N was mathematically computed for 5 kA of discharge, corresponding to MWs of power consumption. Horstman et al. [18] studied magnetohydrodynamic (MHD) acceleration. Using time-of-flight measurements and a thrust stand in atmospheric air experiments, the authors show that reducing the injected mass from 120 µg to 60 µg shifts the system from the highthrust magneto-detonation mode (~20 km/s exhaust velocity) into the more efficient magneto-deflagration regime (~55 km/s). The measured T/P reached around 8 mN/kW for 25µg mass bits. Numerical modelling for micro-plasma thrusters at atmospheric pressure was performed by Rosner and Hemmati [19], yielding T/P around 20 mN/kW, similar to state-of-the-art MPDs that were tested with atmosphere propellants. Wang et al. [20] demonstrated $\sim 8.27 \,\mu\text{N/W}$ T/P using their micro air-fed MPD thruster with an overall efficiency of ~9.4%. All these designs were tested/simulated with air; however, these systems were limited by low sustained thrust, high-voltage and high-current requirements, low T/P, and reliance on external neutralizers or complex array configurations. In contrast, our neutralizer-less self-neutralizing ABPT achieves orders of magnitude T/P and thrust than conventional electric propulsion systems.

The current technologies are designed for altitudes of 120 km and above, with a focus primarily on 200 km (profile is majorly atomic oxygen) and beyond. These altitudes often require the use of air compression or air scoops in front of the thruster [1], [10], [21], [22], introducing additional drag. Some designs may also rely on backup gas tanks using Xenon or Krypton [22]. In this work, we present and characterize an ABPT architecture comprising two stages: a circular arc electron source (CAS) based ionization stage and an MPD acceleration stage. The plasma formation stage is designed to operate in atmospheric air, and the MPD stage utilizes a high-voltage pulse to extract thrust from the pre-ionized air plasma. ABPT is a technology specifically optimized for missions below 100 km. This research indicates that at these lower altitudes, an air scoop is not necessary, simplifying the design and reducing both weight and drag. This enables ABPT to fully utilize atmospheric air as a propellant. The environment below 100 km is less rarefied and more akin to a continuum, offering unique advantages for propulsion efficiency. Additionally, ABPT offers several key advantages. First, it eliminates the need for a traditional propellant tank by utilizing atmospheric air from the upper atmosphere, significantly reducing satellite mass. Additionally, ABPT features a compact, lightweight design, making it ideal for small satellite missions and reducing launch costs. Unlike other air-breathing technologies that require bulky compressors,

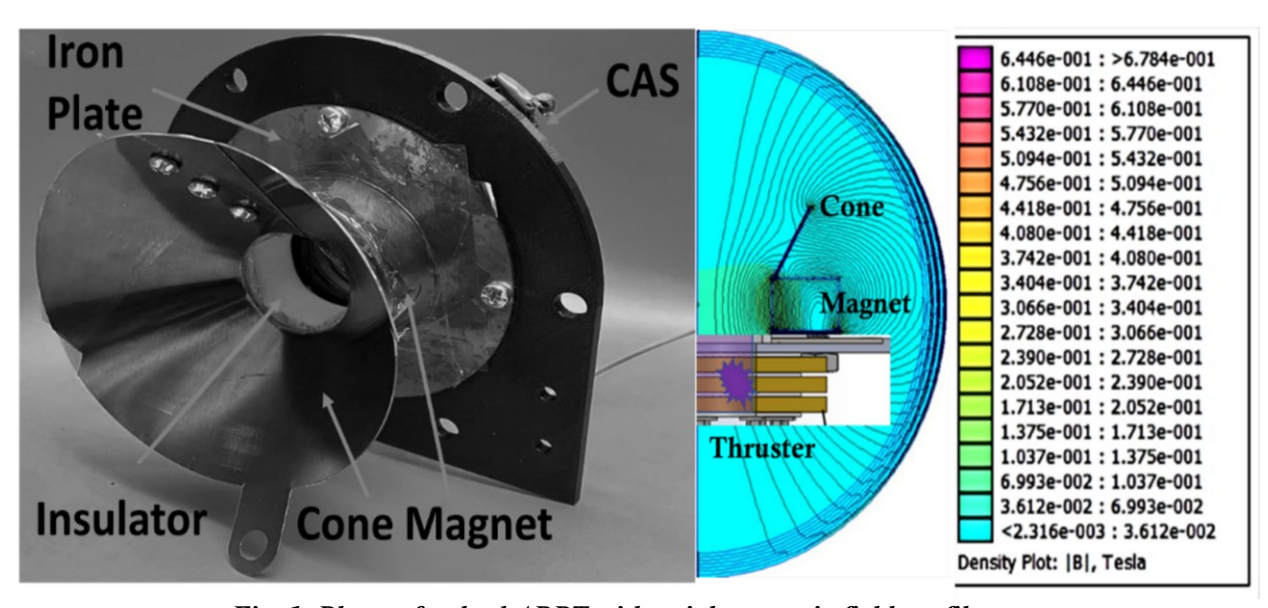


Fig. 1. Photo of pulsed ABPT with axial magnetic field profile.

ABPT employs a hypersonic configuration to generate plasma from incoming air. Furthermore, its self-healing technology [23], integrated into the CAS, improves durability over extended missions.

Finally, ABPT achieves a high T/P ratio, producing thrust levels > 1 N with significantly higher efficiency than conventional electric propulsion systems. This paper describes an experimental campaign to fully assess ABPT. Plasma parameters, including average ion velocity and plasma density, were evaluated using time-of-flight (TOF) and Langmuir probe diagnostics. These were followed by thrust measurements using a torsional beam-based thrust stand [24], [25] to quantify absolute thrust and T/P, demonstrating performance scalability with air flow rates, input voltage, and repetition rate. This integrated approach enables the complete characterization of ABPT, suitable for atmospheric environments. A photo of a pulsed ABPT is shown in Fig. 1. A small CAS [23] was designed with the same inner diameter as the iron plate, ring magnet, and cone. The cathode spot is formed on the cathode and insulator between the two anodes. This cathode spot can rotate under the influence of an axial magnetic field in J (current density) × B (magnetic field) motion and improve its performance [26], [27]. Additionally, to prevent surface barrier discharge between the anode and grid at higher voltages, Teflon rings were added between the anode and grid holder. The arcing over the surface disrupted the electron extraction. At higher air flow rates, high-density plasma will be generated and accelerated due to the Lorentz force. Alternatively, the ring magnet can be replaced with a coil to vary the magnetic field. To reduce power consumption, we have used a permanent ring magnet. The collision of ions and neutrals would result in increased neutral velocity and thrust. The absence of a grid holder and electron extraction grid would result in essentially all of the arc current being extracted. The smaller volume of the source would lead to a higher plasma density. The ions generated in the source would be redeposited in the electrodes, increasing the lifetime of the source. To increase the ionization rate in the CAS, multiple electrodes can be added. The design can be further modified by reducing the radius of the CAS to be less than the radius of the ions and the ion-neutral collision mean free path. The finite element magnetostatics method solver [28] was utilized for performing magnetic simulation in Fig. 1. A permanent magnet placed near the MPD cone (ferrous material) shapes the magnetic field lines, forming a controlled, axially symmetric field configuration. Additionally, between the magnet and the CAS, an iron plate was installed to enhance the radial component of the magnetic field. The color map represents the magnetic flux density (|B|) in Tesla, ranging from below 0.002 T (light blue) to over 0.6 T (magenta), with the highest field concentrations near the magnet and cone interface. This field interacts with the high-current drifting downstream through plasma discharge (J), producing a $J \times B$ Lorentz force that accelerates ions axially out of the thruster. The high current plasma discharge is generated using CAS's electrons interacting with the incoming air flow [23].

II. Materials and Methods

To characterize plasma properties and ion dynamics in the MPD stage of the thruster, a combination of Langmuir probe and TOF measurements was employed (Fig. 1b). The Langmuir probe was constructed using a 1 mm-thick titanium wire, with 2 mm exposed to plasma, while the remainder was shielded using non-porous alumina ceramic. The probe was positioned at both the entrance and exit of the MPD cone to capture spatial variations in plasma parameters. A fixed ion saturation bias of –100 V was applied, and the collected current was measured across a 100 Ω resistor to estimate ion flux. For ion velocity measurements, a TOF diagnostic system was implemented. Given that the ABPT generates air plasma through pulsed arc discharges, the plasma density is strongly correlated with the arc current (I_{arc}) . During operation, modulated arc current spikes generate discrete plasma bunches. Two circular copper wire grids (150 mm in diameter) were placed 12 cm and 24 cm downstream from the thruster exit, both negatively biased to -100 V to suppress electrons and selectively detect positive ions. As the plasma bunches crossed each grid, a sharp ion current spike was induced and recorded across a 500 Ω resistor using a Tektronix oscilloscope. The time delay between the spikes at the two grids, along with the known spatial separation, enabled the calculation of average ion velocities. No external electric field was applied between the grids, ensuring passive ion detection. This combination of Langmuir probe and TOF analysis provides a detailed profile of plasma behavior, ion transport, and effective I_{sp} estimation. To perform thrust experiments, we have utilized our MPNL's torsional beam-based [6], [24] thrust stand modified to measure thrust greater than 1N.

III. Self-neutralization.

As previous research suggests [1], positive and negative ions can be extracted using alternate electric fields to achieve charge density cancellation (neutralization) at the thruster's exit. Extraction

times, anticipated to be in the nanosecond to microsecond range as shown above, aimed to prevent charge accumulation. In this Section, we describe the Particle in Cell Monte-Carlo (PIC-MCC) simulation to describe the process leading to neutralization without an electron neutralizer. The air composition was based on the MSIS-E-90 earth model, which provides the relative concentration of neutral species at altitudes relevant to VLEO. The dominant neutral species considered included N₂, O₂, O, NO, CO₂, H₂O, and trace species like O₃ and OH. All major collision processes (elastic, excitation, ionization, charge exchange, and attachment) involving electrons and ions with these neutrals were incorporated in our Particle-in-Cell Monte Carlo Collision (PIC-MCC) framework. For reaction rates and cross-sections, we referred to our previous work [1] for detailed air plasma kinetics. Neutralizerfree ion thruster is a new research topic of electric propulsion. Two major types of design are now being developed: spatial separation and temporal separation. Separation means that the positively charged ions and the electrons or negative ions are expelled separately. However, we would like to propose a new theory that the ion cloud (Fig. 2) at certain pressure settings, i.e., altitudes, can neutralize itself by utilizing the environment with no extra electrons or negative ions injections. The hypothesis is that the ion charge cloud forms a sufficiently strong electric field, causing electron ionization in addition to photoionization and leading to an avalanche. Such a mechanism can occur at a sufficiently higher pressure and a small mean free path. To simulate such a scenario, a PIC-MCC algorithm with non-local photon collisions has been developed. The simulation is 2D with an initial ion density set at the center (Fig. 3a). The ground (serves as equipotential boundary) is placed slightly above the Z = 0 cm plane, and all other electromagnetic boundary conditions are far field as shown in Fig. 3a. The boundary conditions for species flux are all free for entry and exit. Considering a relatively large mean-free path, there is no need to set up a fine mesh. The simulation has a square and uniform mesh size of 0.2 cm and a time step of 1 ps. It will be shown that an experimental approach involves measuring the floating potential outside the thruster as a function of acceleration voltage, pressure, air flow rate, and electron source energy.

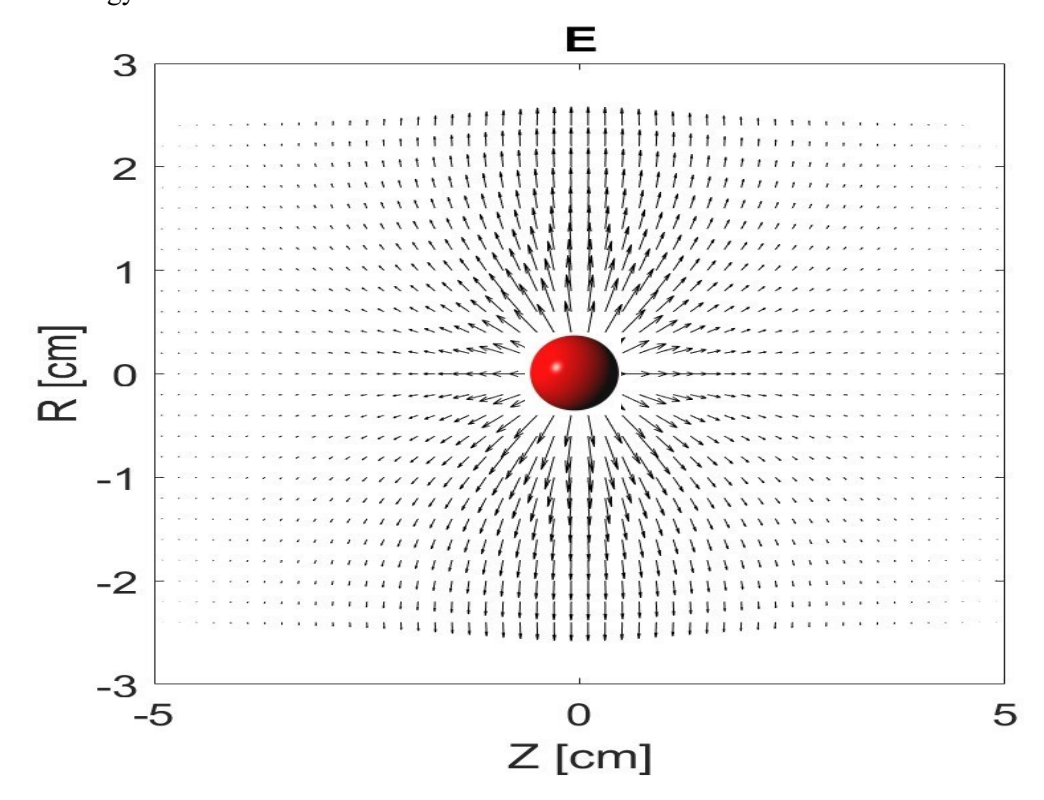


Fig. 2. Spherically symmetrical uniform electric field generated by positive ion cloud is shown. The cloud's strong electric field ionizes background gas facilitated by electron avalanche and electrons in the form of streamers. While the actual ion plumes can extend over several meters, here we have chosen a computational size of centimeters to resolve localized ion cloud effects.

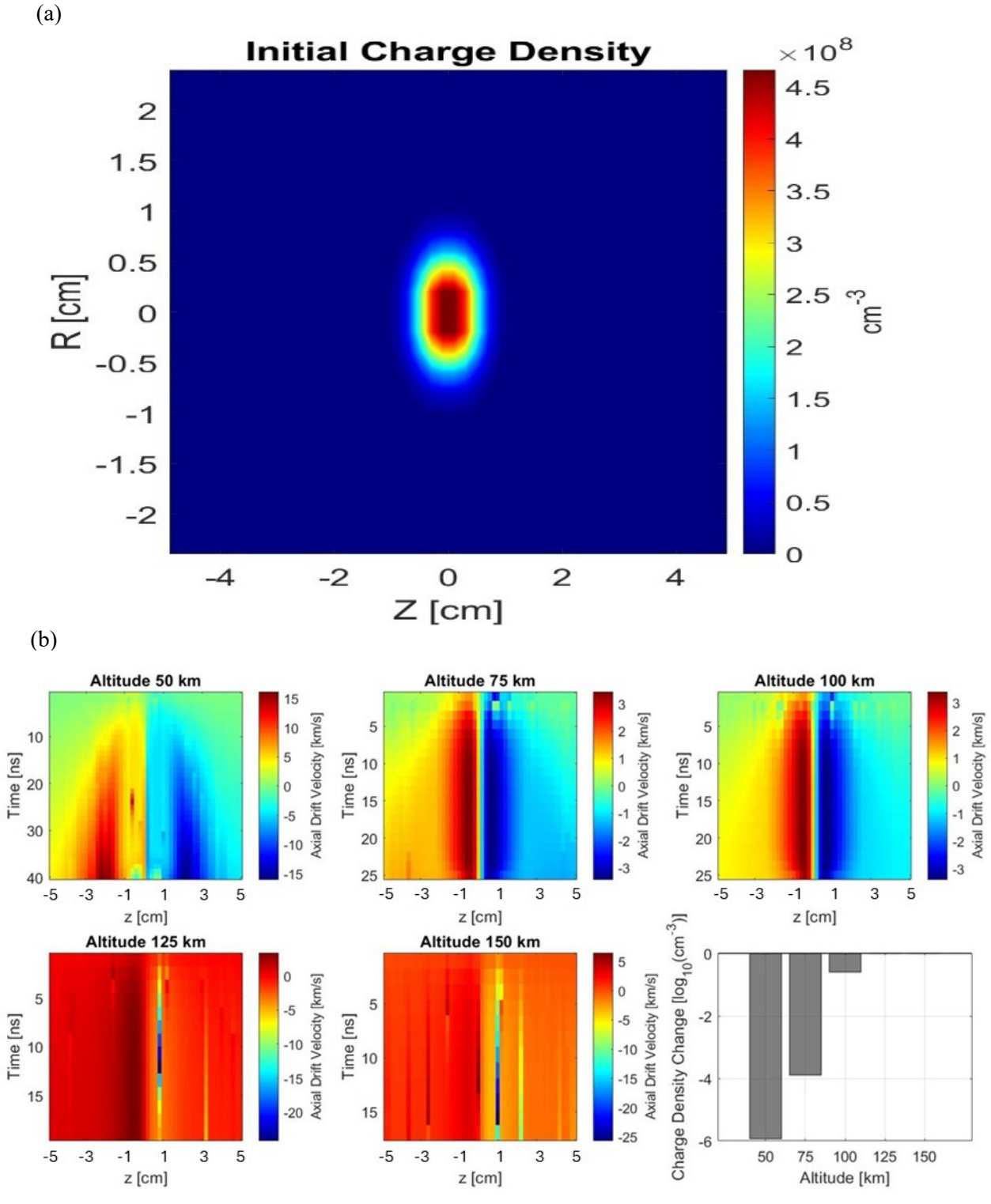


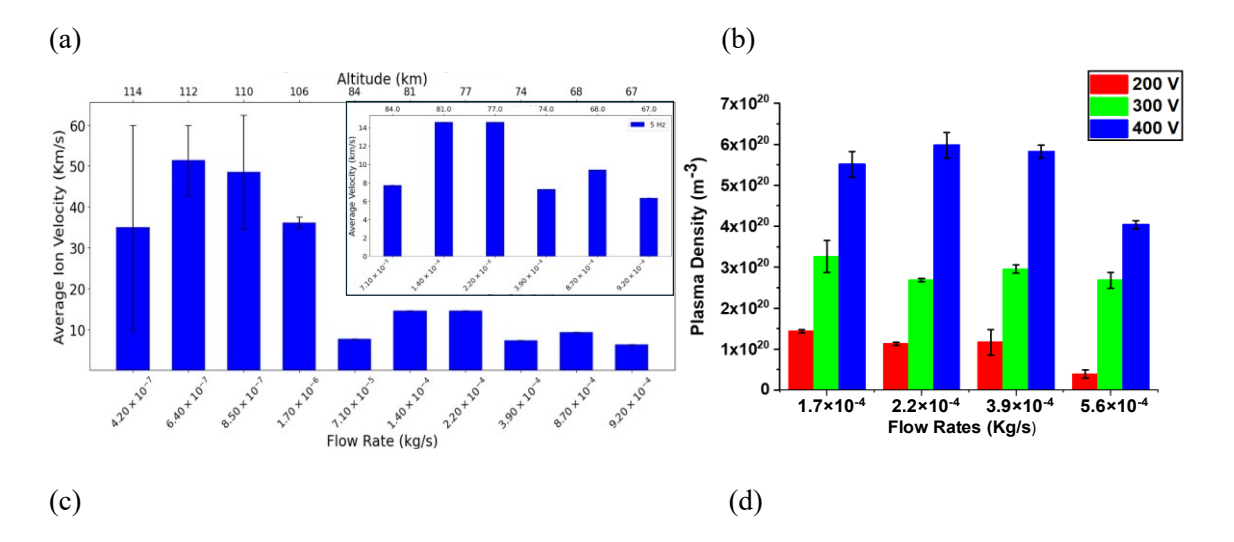
Fig. 3 (a) The initial charge density using PIC-MCC simulation is a Gaussian distribution at the center of a 2D domain. (b) The main results of the simulation at five altitudes. Strong change in

charge densities up to 100 km. The results shown are achieved after the grid convergence study confirmed the stability of our results.

As shown in Fig. 3a, the PIC-MCC simulation shows that the initial ion cloud may have enough electric field to accelerate the electrons and enable them to ionize. The charges consist of N_2^+ and O_2^+ at a ratio of 8:2, while the initial electron density is uniformly distributed at 100 cm⁻³. We used standard air in simulation with all cross sections presented in the Supplementary file. Specifically, the electron-impact collision cross-sections are collected from the "Biagi" database which can be downloaded from the LXCat website. The electron-impact collision rate coefficients are computed using BOLSIG+ (marked in the supplementary file) after inputting the cross-section files into the BOLSIG+ software. A MATLAB code was written to read the data generated from the BOLSIG+ during the simulation. However, the actual ionization rate also depends on the pressure which is determined by the altitude. At a lower altitude (Fig. 3b), such as 50 km, the simulation shows that the electrons gain less energy between collisions. However, due to higher density, the ionization degree keeps increasing, leading to a significant electron avalanche. Finally, substantial electron flux can reach the initial ion cloud and neutralize it leaving newly born ions behind. This is equivalent to the initial positive charges being expanded to a larger area, leading to a less significant ion cloud. When the altitude is higher, the electron energy is higher due to the larger mean free path. This explains why the drift velocity is high at the beginning as shown in the contour plots of 75 km and 100 km in Fig. 3b. However, due to the low density, not enough molecules can be ionized in these cases. Therefore, the equivalent ion cloud expansion and the axial drift velocity expansion are less significant in these cases. At those altitudes, the self-neutralization is weaker. At 125 km and 150 km, such an effect completely disappears. The blip at high altitude is an interesting feature. Due to the low density at such altitudes, the shielding capability of plasma is weak, thus the E field expands more compared to those at low altitudes. At high altitudes, we see more scatter in results. The neutralization degree, defined as the order of charge density decrement compared between the final and initial values is shown in the bar plot of Fig. 3b. Its dependence on the altitude is obvious

IV. Results and Discussion

In this section, the experimental results of the ABPT are presented. Initially, plasma parameters were characterized using a Langmuir probe and TOF measurements to estimate average ion velocity and plasma density. These were followed by direct thrust measurements using a torsional thrust stand to evaluate net thrust and calculate the T/P ratio.



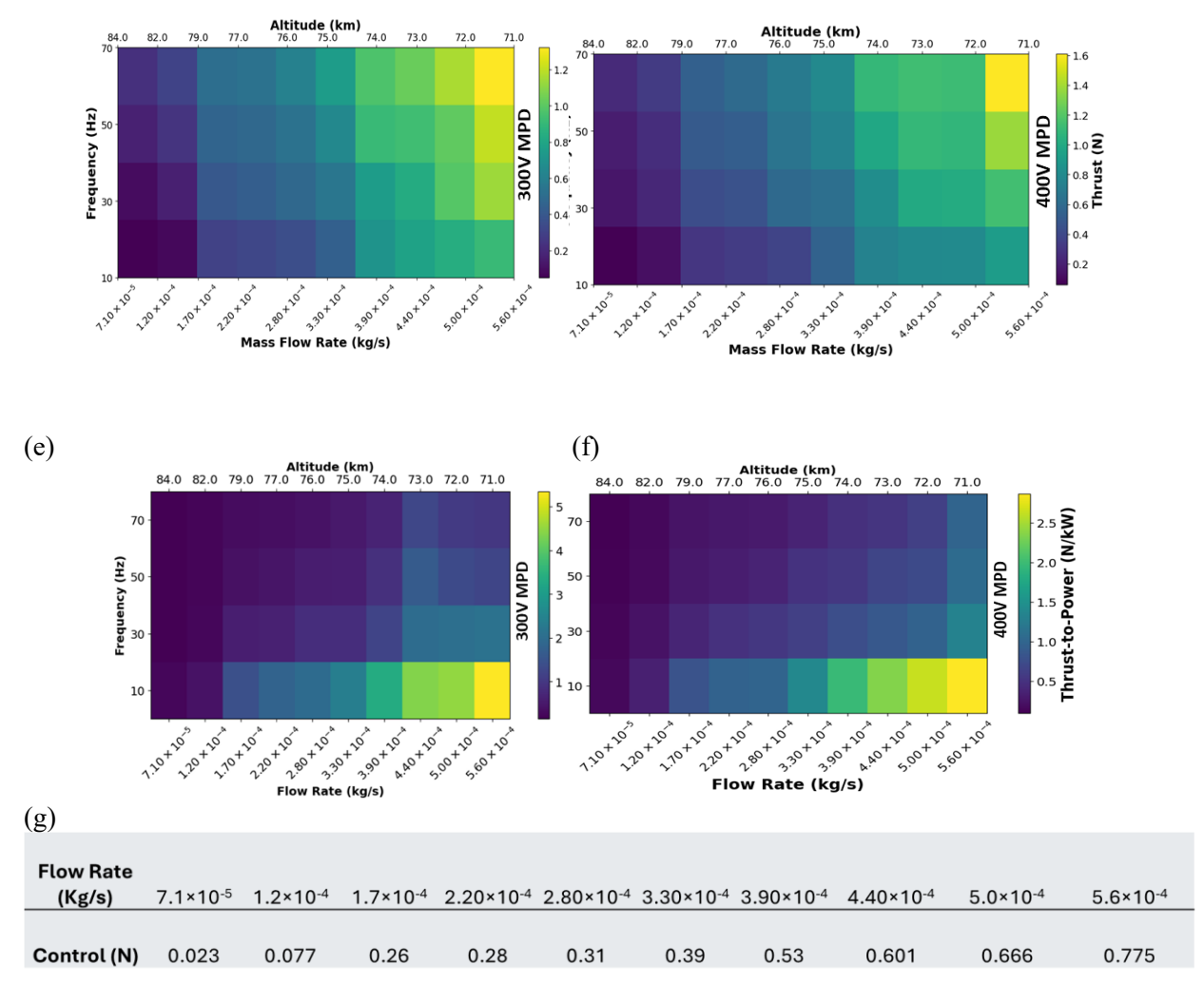


Fig. 4. Variation of plasma parameters with air flow rates in the MPD region of the thruster with second stage voltage as a parameter. (a) Average ion velocity measured using TOF. (b) Plasma density was calculated using a Langmuir probe. The saturated ion current density with an electron temperature of 1-2 eV was used to compute the plasma density. (c-d) The measured thrust and (e-f) T/P are shown under varying mass flow rates and pulsing frequencies. (g) Control force absolute value measured vs gas flow rates. All the above results presented here are obtained after adding 2 additional CASs to the thruster to observe an increase in the total thrust and T/P. Altitude corresponding to specific mass flow rates is shown as well. The experimental mass flow rate was compared with the atmospheric mass flow rate of air flowing through the thruster at 8 km/s (orbital speed) to obtain the altitude. To calculate the atmospheric mass flow rate, altitude vs neutral air density data [29] was utilized.

The experimental results in Fig. 4 illustrate how key plasma parameters—ion velocity (Fig. 4a) and plasma density (Fig. 4b)—vary with air flow rates in the MPD region of the thruster. The TOF shows that the average ion velocity peaks at approximately 60 km/s when the mass flow rate is around 6.4×10^{-7} kg/s (112 km), indicating significant acceleration. At both lower and higher flow rates, ion velocities drop due to reduced ionization efficiency at low flow rates and increased collisional damping at higher pressures. The inset further confirms this trend at a pulsing frequency of 5 Hz, showing a maximum velocity of 14.2 km/s near 1.4×10^{-4} kg/s (81 km) mass flow rate condition and decreasing velocities beyond that. Fig. 4b presents plasma densities measured at the entrance of the MPD acceleration electrode for 200, 300, and 400 V MPD voltage. Plasma density is highest at 2.2×10^{-4} kg/s (77 km) flow rate, reaching values over 6×10^{20} m⁻³ near the cone entrance, and systematically decreases with increasing mass flow rates. At lower MPD voltage (200 V), plasma density remains below 1.5×10^{20} m⁻³ across all conditions due to limited discharge energy. The order of magnitude of plasma density achieved here is in agreement with previously reported results in ref. [11]. The thrust

measurements shown in Fig. 4c-d demonstrate how applied MPD voltage, gas flow rate, and discharge frequency influence the net thrust output of the thruster. For these experiments, the weight of the thruster was too large to be supported on the thrust stand. Consequently, the thrust was measured indirectly by attaching a lightweight plate to the movable torsional arm of the stand [6]. The control was measured from the neutrals, indicating the force of momentum of the neutral gas (thruster off) hitting the plate. The range of control force can be seen in Fig. 4g. The control force can be seen increasing with the mass flow rate (0.022-0.77 N). In all cases, the measured thrust was significantly greater than the control force, indicating strong plasma acceleration. For Fig. 4c-d, thrust increases monotonically with increasing mass flow rate and operating frequency, highlighting the effective coupling between input energy and mass throughput in pulsed discharge regimes. At 300 V (Fig. 4c), the thrust ranges from approximately 0.1 N at low flow rates (~7.1×10⁻⁵ kg/s, 84 km) and 10 Hz to over 1.3 N at the highest flow rate (~5.6×10⁻⁴ kg/s, 71 km) and 70 Hz. The 400 V configuration (Fig. 4d) further boosts thrust output, reaching up to ~1.6 N under the same high-flow, high-frequency conditions, due to stronger Lorentz force acceleration at elevated discharge voltage. T/P plots in Fig. 4e-f highlight the energy efficiency of the thruster across different MPD voltages, frequencies, and flow rates. T/P increases with mass flow rate and tends to show optimal performance at 10 Hz. The experimental P_{exp} power (CAS + MPD power) was calculated using equation (1):

$$P_{exp} = f_D(T_D I_D V_D + T_{MPD} I_{MPD} V_{MPD}) \quad (1)$$

where, f_D (pulsing frequency Hz), T_D/T_{MPD} (CAS/MPD discharge pulse width s), I_D/I_{MPD} (CAS/MPD discharge current A) and V_D/V_{MPD} (CAS/MPD discharge voltage V) are the parameters used for calculations. At 300 V (Fig. 4e), the T/P values peak around ~5 N/kW at flow rates of $\sim 5.6 \times 10^{-4}$ kg/s (71 km), indicating an efficient balance between energy delivery and mass utilization. At 400 V (Fig. 4f), the maximum T/P values are slightly higher, reaching up to $\sim 2.3 \text{ N/kW}$ under optimal conditions. This suggests that higher discharge voltages not only improve absolute thrust but also enhance overall efficiency when properly tuned with mass and frequency input. At higher frequencies, the T/P ratio declines slightly due to increased energy consumption without proportional gains in thrust. At higher mass flow rates, more neutral particles are available for ionization and acceleration, leading to increased thrust. Raising the pulsing frequency results in more pulses per second and higher total power input, which decreases the T/P ratio, showing an inverse relationship compared to thrust. These unusually high T/P values which are well above conventional electric propulsion systems—can be attributed to the air-breathing, hypersonic configuration of the thruster. These findings highlight the significance of employing a hypersonic configuration. It is evident that higher air concentration results in decreased velocity, thereby lowering T/P. To sustain high thrust, using a larger thruster cross-section is necessary to facilitate a higher mass flow rate. Regarding T/P, a high value can be achieved when the inlet velocity is high, and the exhaust velocity is just slightly above the inlet speed.

V. Conclusion

This study demonstrates the operation and diagnostics of MPD-based ABPT tailored for uppermesosphere operations. PIC-MCC simulation showed a strong self-neutralization effect at altitudes between 50 to 100 km. Beyond 100 km, the effect vanishes due to low air pressure. Around 100km, molecular species composition of N_2 and O_2 still dominate, making air a reasonable test gas for preliminary investigation. Langmuir probe analysis yielded electron densities in the order of 6×10^{20} m⁻³ (~2% ionization degree for triple ionization channel CAS ABPT), validating the low-temperature air plasma. TOF measurements indicated ion velocities in the range of 6–60 km/s, corresponding to an estimated I_{sp} between 600–6000 s. The torsional thrust stand recorded previously unseen thrust and T/Paround 1.6 N and 5 N/kW at 300 V MPD acceleration and 5.6×10^{-4} kg/s (71 km) mass flow rate.

Acknowledgments

The authors acknowledge the support of DARPA (Dr. Tabitha Dodson is the program manager). Award no. is HR0011-24-9-0330. The authors also thank Dr. Yevgeny Raitses from Princeton Plasma Physics Laboratory (PPPL) for valuable discussions.

References

- [1] A. Taploo, L. Lin, and M. Keidar, "Analysis of ionization in air-breathing plasma thruster," *Phys. Plasmas*, vol. 28, no. 9, p. 093505, Sep. 2021, doi: 10.1063/5.0059896.
- [2] P. Zheng, J. Wu, Y. Zhang, and B. Wu, *Int. J. Aerosp. Eng.*, 2020, [Online]. Available: https://www.hindawi.com/journals/ijae/2020/8811847/
- [3] M. S. Feldman and R. Spektor, "Air-breathing electric propulsion mission characterization and Design Analysis," in *37th International Electric Propulsion Conference*, 2022. [Online]. Available: https://www.viridianspace.com/wp-content/uploads/2023/05/IEPC-2022-468 Feldman BasicAnalysisABEP-1.pdf,
- [4] P. Crandall and R. E. Wirz, "Air-breathing electric propulsion: Mission Characterization and Design Analysis," *J. Electr. Propuls.*, vol. 1, no. 1, 2022, doi: 10.1007/s44205-022-00009-8.
- [5] M. Tisaev, B. Karadag, and A. Fabris, "Influence of applied magnetic field in an air-breathing microwave plasma cathode," *J. Phys. Appl. Phys.*, vol. 56, no. 46, p. 465203, 2023, doi: 10.1088/1361-6463/acefe2.
- [6] D. B. Zolotuchin, R. S. P. Banduru, K. P. Daniels, I. I. Beilis, and M. Keidar, "Demonstration of electric micro-propulsion multimodality," *Sci. Adv.*, vol. 8, p. 9850, 2022.
- [7] "A First Look at 10cm satellite imagery." [Online]. Available: https://albedo.com/post/albedo-simulated-imagery
- [8] L. Berthoud *et al.*, "Are Very Low Earth Orbit (VLEO) satellites a solution for tomorrow's telecommunication needs?," *CEAS Space J*, vol. 14, no. 4, pp. 609–623, Oct. 2022.
- [9] P. Kansakar and F. Hossain, "A review of applications of satellite earth observation data for global societal benefit and stewardship of planet earth," *Space Policy*, vol. 36, pp. 46–54, May 2016.
- [10] K. Diamant, "A 2-stage cylindrical Hall thruster for air breathing electric propulsion," in 46th AIAA/ASME/SAE/ASEE Joint Propulsion Conference and Exhibit, 2010.
- [11] L. Pekker and M. Keidar, "Analysis of airbreathing hall-effect thrusters," *J Propuls Power*, vol. 28, no. 6, pp. 1399–1405, Nov. 2012.
- [12] G. Ferrato and Piragino, "Andrenucci and Andreussi, Development Roadmap of SITAEL's RAM-EP System." 2019. [Online]. Available: http://electricrocket.org/2019/886.pdf
- [13] M. R. La Pointe, "High Power MPD Thruster Performance Measurements." [Online]. Available: https://ntrs.nasa.gov/api/citations/20040139544/downloads/20040139544.pdf
- [14] B. B. Donahue I and J. Boise Pearson, "Advanced plasma propulsion for human missions to Jupiter." [Online]. Available: https://ntrs.nasa.gov/api/citations/20000013636/downloads/20000013636.pdf
- [15] C. Adkins, D. Belcher, M. Akhter, A. Duggleby, N. D. Cardwell, and D. Staack, "Design and optimization of a high thrust density air-breathing pulsed plasma thruster array," *J Elect Propuls*, vol. 3, no. 1, Sep. 2024.
- [16] B. Göksel and I. C. Mashek, "First breakthrough for future air-breathing magneto-plasma propulsion systems," *J Phys Conf Ser*, vol. 825, p. 012005, Apr. 2017.
- [17] I. McKinney and J. Murnan, "Revolutionizing spaceflight: A study on electric propulsion and air-breathing MPDs," *J Stud Res*, vol. 10, no. 2, Aug. 2021.
- [18] E. Horstman, A. Woodley, and T. C. Underwood, "Magnetohydrodynamic operating regimes of pulsed plasma accelerators for efficient propellant utilization," Mar. 2025.
- [19] A. Rosner and A. Hemmati, "Numerical modeling of air plasma flow in air-breathing microplasma thrusters at atmospheric pressure," *J Elect Propuls*, vol. 4, no. 1, May 2025.
- [20] Z. Wang, Y. Eun, and X. Wu, Design and demonstration of a micro air-fed magnetoplasmadynamic thruster for small satellites.
- [21] D. Cara *et al.*, "RAM Electric Propulsion for Low Earth Orbit Operation: an ESA Study." 2007. [Online]. Available: http://electricrocket.org/IEPC/IEPC-2007-162.pdf
- [22] Andreussi, "A review of air-breathing electric propulsion: from mission studies to technology verification"," *J. Electr. Propuls.*, vol. 1, no. 31, 2022, doi: 10.1007/s44205-022-00024-9.
- [23] A. Taploo, V. Soni, and H. Solomon, "Characterization of a circular arc electron source for a self-neutralizing air-breathing plasma thruster," *J Electr Propuls*, vol. 2, p. 21, 2023, doi:

- 10.1007/s44205-023-00058-7.
- [24] J. Kolbeck, T. E. Porter, and M. Keidar, *High precision thrust balance development at the George Washington 35th Int. Electric Propulsion Conf. Georgia Institute of Technology*. Atlanta, Georgia, USA, 2017.
- [25] D. B. Zolotukhin, K. P. Daniels, S. R. P. Bandaru, and M. Keidar, "Magnetoplasmadynamic two-stage micro-cathode arc thruster for CubeSats," *Plasma Sources Sci Technol*, vol. 28, no. 10, p. 105001, Oct. 2019.
- [26] T. Zhuang, A. Shashurin, I. Beilis, and M. Keidar, "Ion velocities in a micro cathode arc thruster," *Phys. Plasmas*, vol. 19, no. 6, p. 063501, 2012.
- [27] A. Taploo, "Self-neutralizing air breathing plasma thruster for very low earth orbits." [Online]. Available: https://www.proquest.com/openview/be12c127f8814884ffac890c11f73d39/1?pq-origsite=gscholar&cbl=18750&diss=y
- [28] "Finite element method magnetics femm.info." pp. 6-8, 2022. [Online]. Available: https://www.femm.info/Archives/doc/manual42.pdf
- [29] "MSIS-E-90 Atmosphere Model , https://ccmc.gsfc.nasa.gov/modelweb/models/msis_vitmo .php." 2021.